

Tutorial

Effective AVO crossplot modeling: A tutorial

Christopher P. Ross*

ABSTRACT

The ability to crossplot attributes from a 3-D seismic volume permits a geophysicist to identify and high grade subsets of the 3-D volume that warrant detailed inspection. In the case of amplitude-variation-with-offset (AVO) crossplotting, the seismic attributes are derived from CDP data. Crossplotting has become a fundamental process in AVO analysis, just as it is in petrophysical analysis. Comprehending the intricacies and selection of attributes is essential for successful AVO analysis and improved seismic interpretation.

AVO crossplotting of modeled seismic data derived from well logs with the Biot-Gassmann equations provides a basis for understanding fluid substitution effects on AVO attribute interactions when crossplotting. With these model-based understandings, improved multi-attribute interpretation processes can commence with AVO crossplotting of seismic volumes.

INTRODUCTION

With the proliferation of professional talks and publications regarding amplitude-variation-with-offset (AVO) crossplotting, the technique is widely being accepted as an important facet in AVO analysis. Seismic (AVO) crossplotting can be a diagnostic tool for classifying AVO responses (Foster et al., 1993; Castagna and Swan, 1997; Castagna et al., 1998), and for identifying hydrocarbon deposits when performed correctly (Ross, 1995; Verm and Hilterman, 1995). However, as with all AVO studies, *a priori* information is crucial, since it serves as a benchmark between prospect and analogy.

The need for seismic crossplotting arises from the complexities of the subsurface, the nonuniqueness of elastic seismic responses, and the desire to display multiple attributes simultaneously. In general, the primary attributes extracted for AVO

analysis are the intercept and the gradient, which are obtained from velocity corrected CDP records. A general description of the extraction of AVO attributes is presented in Appendix A. These base attributes (intercept and gradient) can be used independently, combined through a mathematical process to generate a computed AVO attribute, and/or crossplotted against one another to determine anomalous responses that may be associated with a particular lithology or pore fluid of interest.

Figure 1a is a relative amplitude processed seismic profile from the Gulf of Mexico shelf, traversing a known hydrocarbon-charged reservoir (bright spot). Figure 1b is the color-coded seismic display of Figure 1a illustrating the AVO response using typical AVO crossplotting techniques. The actual crossplot used to determine the anomaly in Figure 1b is shown in Figure 1c with the AVO intercept plotted along the abscissa and AVO gradient along the ordinate. Each point in the crossplot is mapped using the amplitude of the intercept (*A*) and gradient (*B*), and each pair in this display are color-coded using two-way time. Although there are noticeable patterns or trends (possibly two trends), the meaning of these patterns is unclear without AVO modeling and model-based crossplotting. AVO modeling (construction of nonnormal incident synthetic seismograms from well logs) is a fundamental part of the benchmark process because it permits direct (or nearly direct) correlation of lithology and pore fluid measurements with observed seismic data. This is why AVO modeling is important—to understand which AVO responses are indicative of hydrocarbon-charged pore fluids or pertinent lithologies. This article presents a straightforward methodology incorporating AVO crossplotting into AVO modeling.

AVO MODELING TO CROSSPLOTTING

The procedures for this modeling technique are straightforward. The requirements for successful implementation are a fundamental understanding of pore fluid effects on rock properties, knowledge of the pore fluid and lithologic (mineralogy) relationships with the seismic response, the identification and

Manuscript received by the Editor January 21, 1999; revised manuscript received September 3, 1999.

*Hampson-Russell Software Services (U.S.) Inc, 3000 Wilcrest, Suite 170, Houston, Texas 77042. E-mail: cross@hrs-us.com.

© 2000 Society of Exploration Geophysicists. All rights reserved.

extraction of the appropriate AVO attributes from the models, and seismic crossplotting of the AVO attributes. The typical modeling flow will involve the following steps:

- 1) Edit and prepare the well logs for AVO modeling.
- 2) Create fluid/lithology replacement well logs.
- 3) Generate an in-situ and a fluid/lithology replacement AVO model.
- 4) Generate the appropriate AVO attributes for both models (intercept and AVO gradient, for example).
- 5) Crossplot the attributes from each model simultaneously.

I describe these steps in more detail and conclude with a closer examination of how reservoir changes affect a crossplot's appearance.

Steps 1 and 2—Well log preparation for in situ and fluid replacement modeling

For this example, I have selected a potential bright spot example from the deepwater Gulf of Mexico. The in-situ pore fluids of the reservoir are brine (water), and the clean, well-sorted sandstone reservoir has a porosity of approximately 34%. Encasing the reservoir are shales (mudstones). Performing standard log analysis techniques to "quality control" the well logs prior to modeling is always recommended and

often results in more accurate models. Common log editing procedures should involve a quality control assessment of the compressional sonic, bulk density, and shear-wave sonic logs if available, since these are the direct input wireline logs for AVO modeling. Environmental effects, hole effects, and mechanical/operating corrections (such as logging speed and gain adjustments) can affect log responses, and corrections for these effects should be rendered whenever possible. If such corrections are not possible, the reliability of the modeled results should be scrutinized carefully.

Shear-wave sonic logs.—If a shear sonic or Poisson's ratio log is not available, then one can be constructed for wet sands and shales (or other lithologies) using a variety of techniques. Excellent sources of reference regarding shear-sonic construction are Greenberg and Castagna (1992) and Castagna (1993), which summarize lithology-based regression. Note that algorithms using regression-based approaches are often not accurate through reservoirs with gas or oil present, and care should be taken when computing shear sonic logs through these reservoirs.

Another approach for constructing shear sonic logs involves the use of multilinear regression or artificial neural network techniques (for example, Arbogast et al., 1997). If a sufficient well population containing compressional sonic, shear sonic,

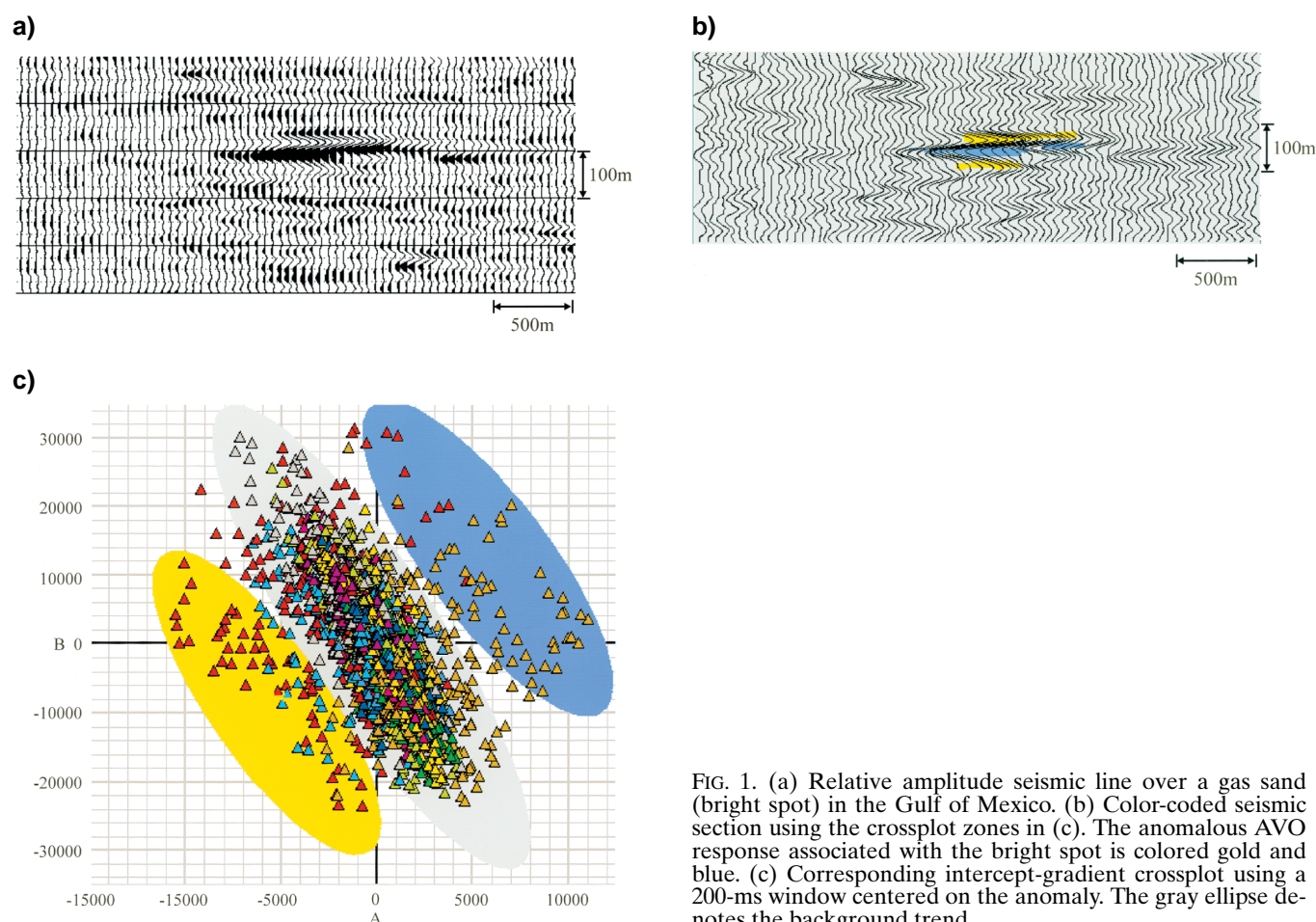


FIG. 1. (a) Relative amplitude seismic line over a gas sand (bright spot) in the Gulf of Mexico. (b) Color-coded seismic section using the crossplot zones in (c). The anomalous AVO response associated with the bright spot is colored gold and blue. (c) Corresponding intercept-gradient crossplot using a 200-ms window centered on the anomaly. The gray ellipse denotes the background trend.

and other wire line logs in the same geological setting exists, a training set can be developed using common wireline suites to generate a shear sonic log at the well lacking an in-situ measurement. If the training set includes a representative number of hydrocarbon-filled reservoirs, the multi-attribute technique may generate an accurate shear response in these zones as well. The readers are directed towards the aforementioned references for more details on shear sonic log construction through hydrocarbon reservoirs.

Comments on observed versus computed shear sonic data.—There is still some debate in the oil and gas industry about the reliability of observed shear-sonic measurements (for example, Hatchell, 1993). Some individuals question the validity and repeatability of the measurements, while others feel the more cost effective approach is to compute the shear sonic from other recorded logs. I suggest acquiring shear sonic data whenever possible and evaluating the sonic quality prior to modeling. This is a philosophical position. Since the cost of acquiring the shear sonic log is much smaller than drilling an intermediate or deep well and since ability to sample the subsurface is only available for a short interval, I feel the benefits outweigh the relatively small expense of acquisition especially if the results are meaningful. One can then evaluate its quality prior to modeling. If the data is of good quality, incorporate it in to the modeling, and share the information with reservoir engineers. If it is not satisfactory, create one using numerical techniques similar to the aforementioned techniques.

In this example, an in-situ shear wave log was not available, so one was computed using a sand percentage index constructed from the gamma-ray, SP, and neutron porosity logs. The Poisson's ratio log was created using a lithology-based regression, and calibrated with observed Poisson's ratio measurements in the area. (Average values for Poisson's ratio for shales is 0.40, and for clean, wet sands, 0.38.) Comparison of the computed shear log with observed shear logs in the area indicate the computation is acceptable.

Fluid replacement substitution.—Fluid replacement of in-situ pore fluids is common practice in AVO modeling. Domenico (1976), and Murphy et al. (1993) discuss the general Biot-Gassmann-Gertsma (BGG) equations typically used for fluid replacement. Using the BGG equations, wireline responses of density and sonic logs through reservoirs with water or brine-charged pore fluids can be computationally altered to estimate hydrocarbon-charged pore fluids. Although the reverse replacement process (hydrocarbon-charged pore fluids to water-filled) is possible, wireline log data is sometimes biased by mechanical and physical limitations of wireline measurements through hydrocarbon-bearing (gas) reservoirs. Therefore, fluid substitution of water for in-situ gas or oil should be performed with care and calibrated to observed responses wherever possible.

The original, brine-filled reservoir ($S_w = 1.0$) in this example is at 12 800 ft (3900 m) was altered to a water saturation of 0.40. The well logs and the objective (yellow zone) are presented in Figure 2 with the in-situ properties displayed in black and the fluid replacement logs displayed in red. Strong decreases in compressional velocity (sonic), bulk density, and Poisson's ratio are observed in the fluid replacement logs, which are typical for low acoustic impedance bright spots in unconsolidated Ter-

tary strata. Poisson's ratio values approach 0.20 for the fluid replacement (gas-charged) reservoir. Only the pore fluid in the reservoir was replaced, and no other lithology or fluid replacement changes were performed. As previously mentioned, the reservoir is overlain by approximately 600 ft (180 m) of shale and overlies another 150 ft (46 m) of shale.

Steps 3—AVO modeling

There are many algorithms available for forward modeling (synthetic seismogram generation). For isotropic media, these modeling algorithms can be grouped into two classes, ray-trace based and wave-equation based. Zoeppritz equations (Aki and Richards, 1980) and a linearized version of Zoeppritz equations are the most common ray-traced-based modeling programs. The linearized version has been advocated by Simmons and Backus (1994) as more accurate by accounting for the locally converted shear wave. However, the difference between the two ray-based (Zoeppritz) methods may not always be

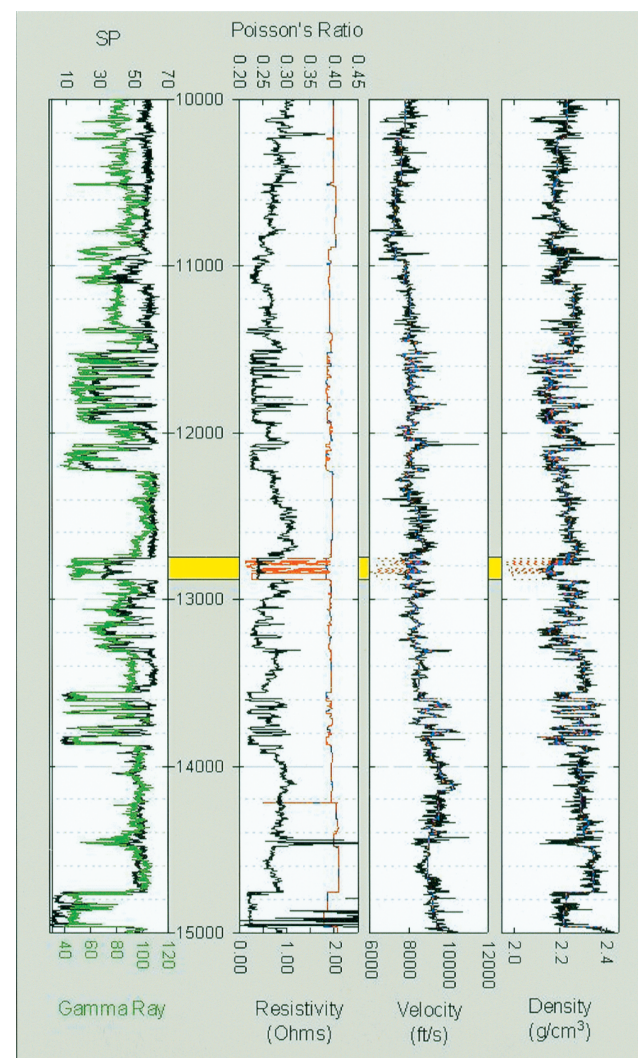


FIG. 2. Wireline well log suite for the AVO modeling example. The reservoir to be examined has been annotated in yellow. In-situ values are in black, fluid replacement values in red. Depths are in feet.

significant, depending on the relative thicknesses of the reservoir and encasing strata modeled. Whereas ray-trace approaches are computationally faster than wave equation methods, wave equation methods produce better accuracy since they better approximate the observed subsurface wave propagation by including multiples and converted-wave responses.

AVO modeling in this paper is performed using a full elastic wave-equation modeling algorithm based on the work of Kennett (1979), and both AVO models (in situ and fluid replacement) include geometrical spreading losses, transmission losses through interbedded multiples, P - SV converted-waves, and primary multiples. After finely blocking the sonic (compressional), density, and Poisson's ratio curves (Figure 2), a flat elastic model is constructed and a full offset synthetic seismogram generated. A zero-phase, trapezoidal 4/8–24/48 Hz wavelet was used, and offsets from 1000 to 20 000 ft (300 to 6100 m) were modeled. These offsets are typical of current acquisition being performed in the area, and with an offset-

to-depth ratio of 1.6 are more than sufficient to see the full, subcritical AVO responses. It is important to avoid apertures that are too restrictive (those with low offset-to-depth ratios) that will give ambiguous results (see Ross, 1997, for example). Likewise, the bandwidth reflects an adequate frequency range for the reservoir depth.

With the algorithm employed to generate these models, data blocking is not required. The data is only blocked to increase the computational efficiency. How accurately the model portrays the subsurface depends on how well the model resembles the subsurface. In this example the fine blocking [10 ft (3 m) average block size in the area of the reservoir] yields very accurate results, when compared to unblocked test results.

Step 4—Performing AVO analysis (crossplotting preparation)

One can easily take each AVO (in-situ and fluid-replacement) model, extract AVO attributes, and crossplot the results

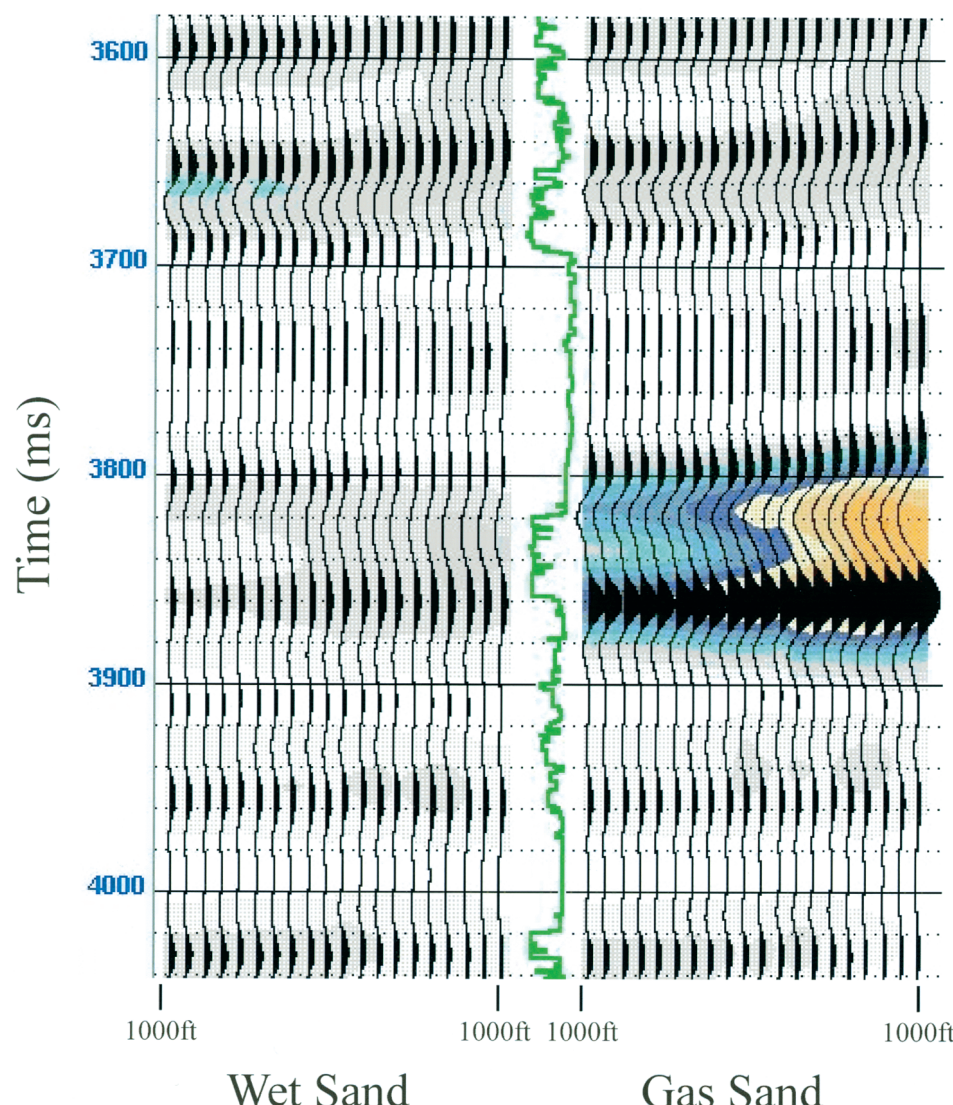


FIG. 3. Forward models from the full elastic wave-equation algorithm. In situ (left), a time-based gamma ray log (center), and gas fluid substitution (right). The offsets for each record range from 1000 (left) to 20 000 ft (right). Colors represent the envelope amplitude. The anomalous AVO response is apparent in the gas substitution model.

separately, but a better understanding can be obtained if the models are crossplotted simultaneously. After all, this is what one would see analyzing an observed seismic record. To do this, I have taken both modeled CDPs and merged them into one line and loaded them as a small, two-CDP survey (Figure 3). In Figure 3, the first CDP is the in-situ (wet) model, the second CDP is the fluid-replacement (gas) model. A time-based gamma-ray log has been inserted between the two CDPs for reference. While a nearly constant AVO response is observed for all the wet sand/shale interfaces in both models, an increase in amplitude variation with offset is readily observable in the second CDP, as denoted by both the amplitude excursion of the wiggle traces and by the variable intensity color displays. The weaker envelope amplitude (blue) increases to larger values (orange) from near to far offsets for both the top (trough) and the base (peak) of the reservoir.

AVO attributes.—A decade ago, most geophysicists would have stopped at this point and looked for similar responses in recorded (2-D) CDP gathers, but with the advent of large 3-D volumes being used for AVO analysis, searching the volume for individual CDP responses can be a daunting task. To expedite this formidable challenge, attribute volumes are typically constructed for detection of AVO anomalies, either in typical time section (in-line and cross-line) analysis or with horizon slices.

A fundamental question one must ask is which attribute to use. Although two primary attributes are extracted from the CDP gathers [the intercept (A) and gradient (B)], often the two attributes are combined (i.e., $\alpha A + \beta B$, where α and β are scalars) to form a single attribute, displayed as a CDP stacked volume. However, interpretation of single attribute AVO volumes can sometimes be ambiguous. An alternate approach is to crossplot the A and B attributes and look for visual anomalies on the resulting crossplot (A - B plane). But, before this A - B plane can be interpreted in a meaningful way, AVO crossplot modeling is necessary to determine what crossplot relationships exist (if any) between hydrocarbon-bearing reservoirs and wet reservoirs, or other lithologies such as tighter sands, silts, and calcareous-cemented sands. (These ambiguities and uncertainties again demonstrate the need for the careful study of AVO attributes and crossplotting.)

AVO extraction.—Using a smoothed version of the sonic log from the in-situ well, average incident angles can be estimated, and A and B generated for both CDPs. (See Appendix A for a review of AVO attribute extraction.) For display purposes, I show the A term as a wiggle, and a combined AVO attribute term as a variable intensity color display. In Figure 4, the conventional AVO product ($A*B$) is the color attribute. In Figure 5, the attribute is the scaled Poisson's ratio change, which is a weighted sum of the A and B terms. This is equivalent to the Smith and Gidlow's (1987) fluid factor for nearly invariant V_P/V_S windows, and is similar to the $(A+B)/2$ attribute as discussed by Castagna and Smith (1994). (See Appendix B for discussion on the scaled Poisson's ratio attribute being equivalent to the fluid factor.) The top and bottom of the gas sand modeled in the second CDP is denoted in the AVO product as blue and magenta, and in the scaled Poisson's ratio display as orange (negative) and yellow (positive). The scaled Poisson's ratio attribute has been scaled to emphasize the hydrocarbons

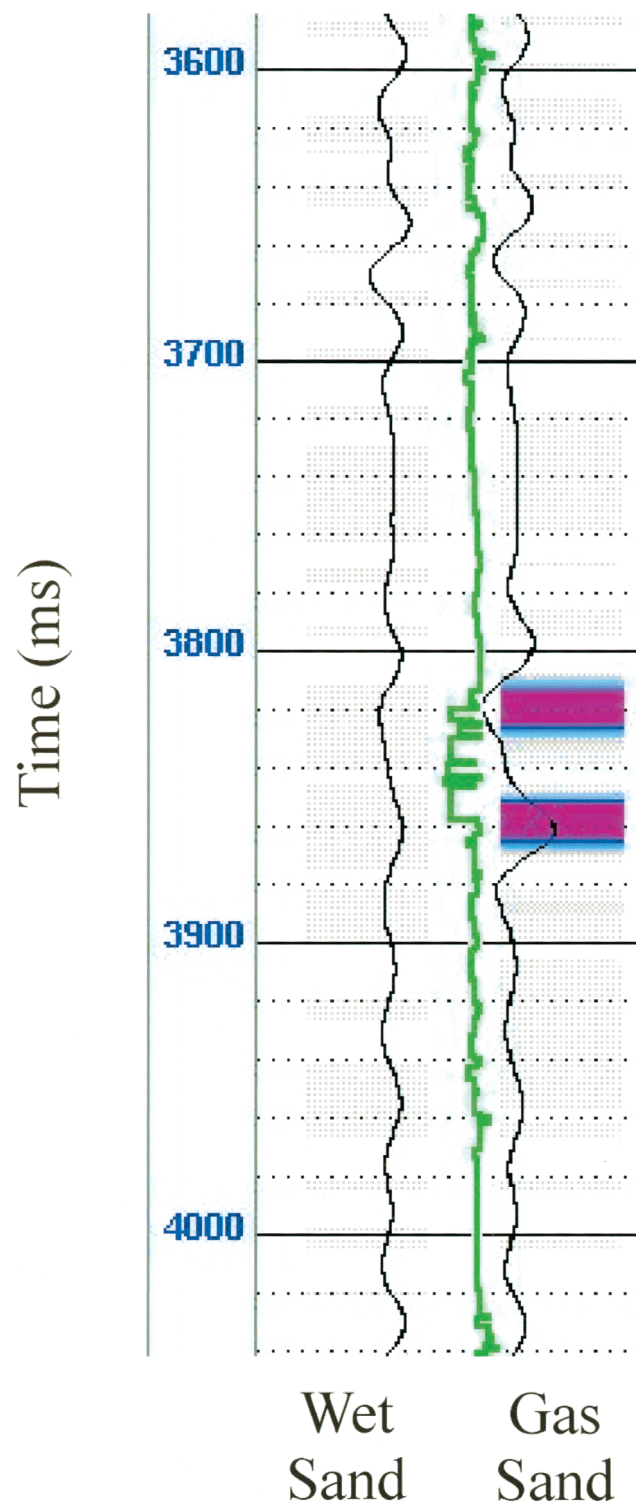


FIG. 4. AVO computation from the gathers in Figure 3. The intercept (A) is presented in trace display (wiggle), the AVO product ($A*B$) is displayed as variable intensity color. The in-situ model is left, the time-based gamma ray center, and the gas-substitution model right. Magenta and blue shades indicate strong positive values that are associated with the modeled gas reservoir.

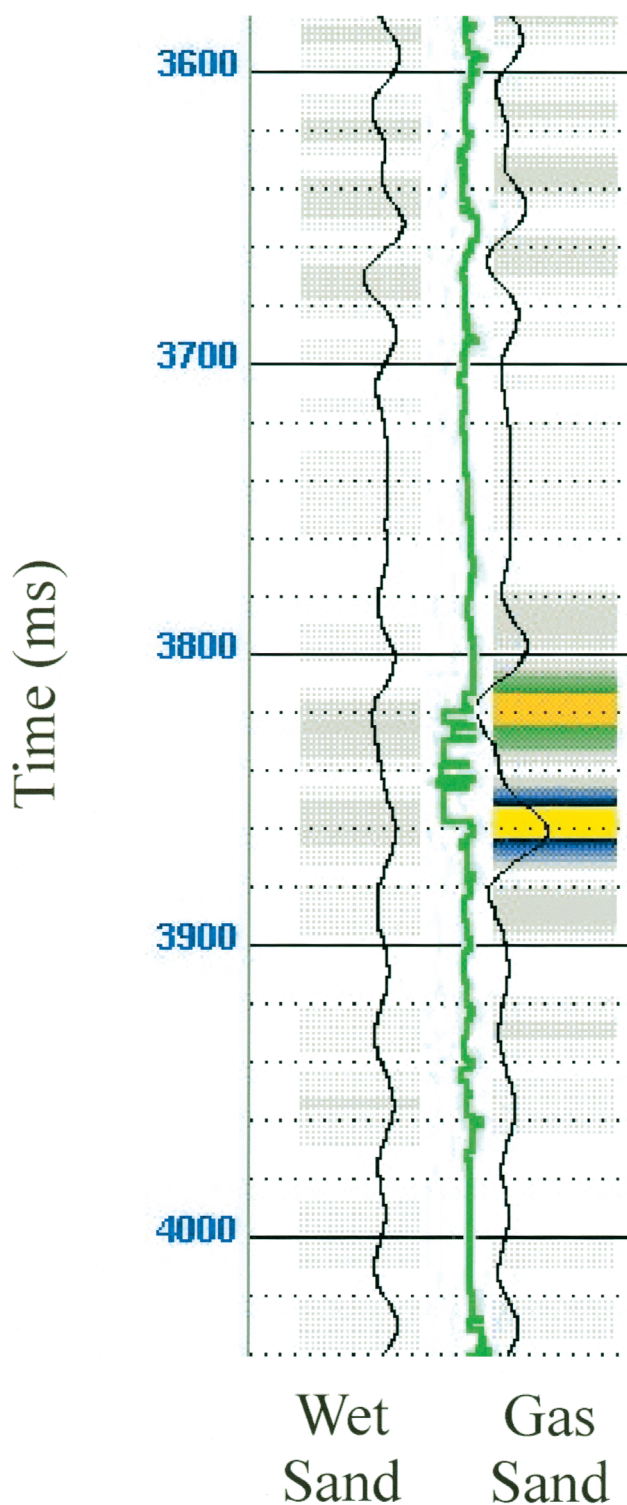


FIG. 5. AVO attributes with the intercept as the wiggle overlay and the scaled Poisson's ratio change attribute ($\alpha A + \beta B$) in color. The yellow and orange colors indicate anomalous AVO responses. As in Figure 4, only the fluid replacement model at the reservoir exhibits an AVO response. Values for α and β are 0.5 and 0.31, respectively.

at this time and depth. Scalars of 0.5 and 0.3 were used for the A and B attributes, respectively. The scalar values were determined interactively by comparing the wet sand/shale response to the gas sand/shale response. Both figures show strong AVO anomalies where the gas substitution was performed in the second CDP (trace 2), and both figures exhibit low amplitude (background) responses for the in situ model (trace 1).

Again, one could stop at this point and compare the modeled single attribute responses directly to the data. However, crossplotting all the data can help identify anomalous responses and possibly present a better understanding of the lithology or pore fluid variation.

Step 5—Crossplotting AVO attributes

Using the extracted A and B attributes, the wet intercept-gradient trace pair and a gas (modeled) trace pair can be crossplotted together in the A - B plane. Figure 6 is the AVO crossplot of both models [CDP 1 (in-situ model) and CDP 2 (fluid-replacement model)] using a 600-ms window centered at 3840 ms and a 4-ms sample rate. For observed seismic data the crossplot should be computed using an interpreted horizon rather than a constant time (3840 ms, for example); however, for a flat model, this will be equivalent. Green points in the crossplot correspond to A - B pairs from the in-situ CDP, the purple points for the gas-substitution CDP.

Interpretation of the crossplot.—The crossplot was analyzed by interpreting clusters or patterns. This can be performed using numerical techniques (such as discriminant analysis) or visually. In this example, I have manually (visually) determined the clustering. The crossplot was interpreted in the following manner: the gray ellipse denotes wet sand and shale interfaces (background reflectors), and the blue and gold colors illustrate

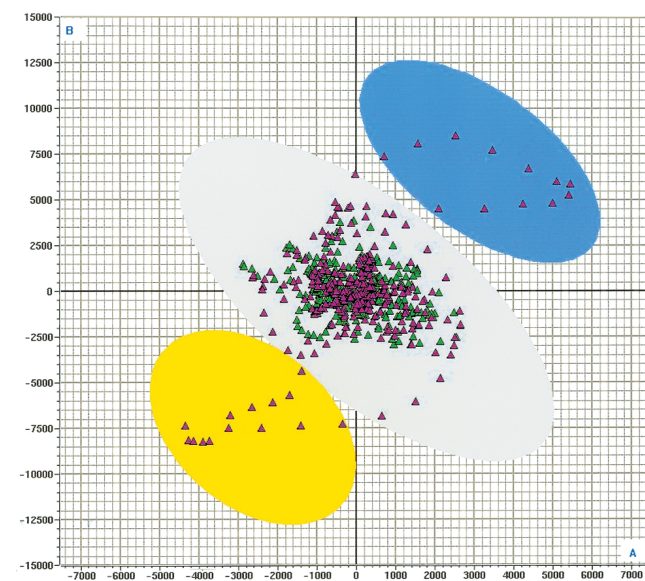


FIG. 6. AVO crossplot of the intercept and gradient from the in-situ model (green points) and gas-substitution model (purple points). The gray ellipse indicates the wet sand/shale background response, the blue and gold ellipses highlight A - B pairs that are anomalous.

anomalous intercept-gradient pairs. Notice that all of the green points from the in-situ model lie within the gray background ellipse, as do most of the points from the gas-substitution model (purple). A few points from the second CDP lie outside of the background ellipse, and these anomalous points are from the gas sands inserted into the second model. The gold ellipse highlights the top of the gas sand (trough), and the intercept-gradient pairs that correspond to the base of the sand (peak) lie within the blue ellipse.

In Figure 7, the color-coded points from the crossplot are mapped back to a trace display. From this figure and Figures 4 and 5, it is clear that the anomalous crossplot points (those pairs lying in the blue and gold ellipses) that lie off the background trend define the modeled gas sand.

Estimating Poisson's ratio from a crossplot.—It has been demonstrated that crossplotting in the A - B plane can be diagnostic in identifying lithologies (for example, Foster et al., 1993). Furthermore, Castagna and Swan (1997) and Foster et al. (1997) demonstrate that the slope of the background trend in the A - B plane is determined by the V_P/V_S ratio. For a V_P/V_S ratio of 2.0 (Foster et al., 1997) show that the background trend follows the fluid line. As V_P/V_S ratios move away from 2.0, the wet sand and shale A - B pairs follow the corresponding fluid lines, and the goodness of fit to the fluid line decreases.

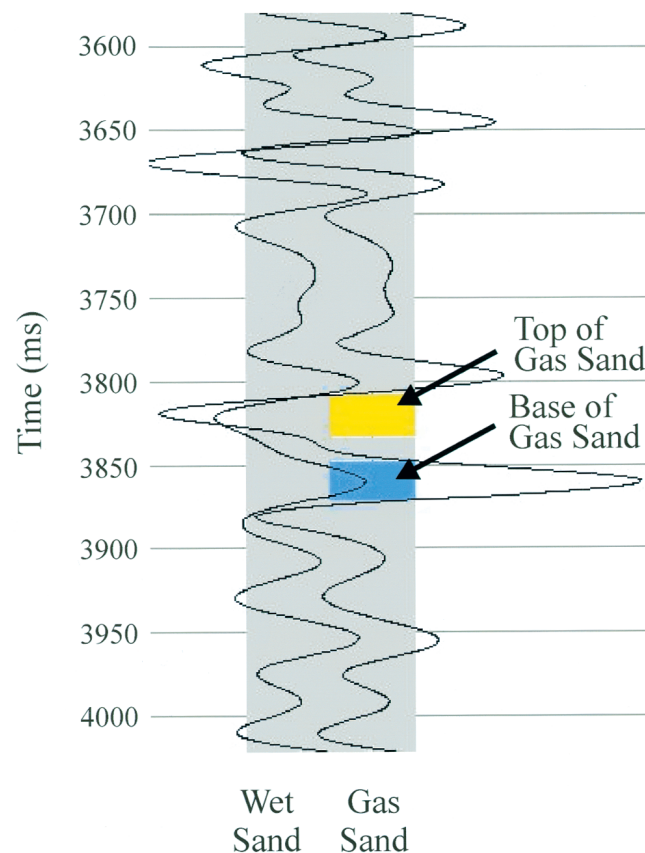


FIG. 7. Seismic wiggle display of the A trace in each model with the color zonations from the crossplot in Figure 6 shown in the background. Notice the anomalous ellipses from the crossplot (blue and gold) correspond to the gas sand model, whereas all other sands and shales are considered background.

By measuring the slope of the fluid line, a V_P/V_S ratio and Poisson's ratio for the wet sands and shales can be determined. Linear regression of just the A - B pairs in the gray ellipse (the background trend) indicates that $B = -0.379A + 25.35$. Foster et al. (1997) defines the slope (for $V_P/V_S = 2.0$) as $1 - 8\gamma^2$, where γ is the V_S/V_P ratio. Using the determined slope (-0.379) and solving for γ using the V_P/V_S approximation of 2.0, I estimate Poisson ratio of the background trend to be 0.40. As one might expect, this corresponds well with the input Poisson's ratio used to generate the model. This may seem circular, however, being able to estimate Poisson's ratio from the crossplot allows one to determine the scalars for the scaled Poisson's ratio attribute. For the Poisson's ratio determined from the crossplot, the scalars for A and B are 0.50 and 0.33, respectively. These values are very similar to the empirically scaled values used in the scaled Poisson's ratio attribute. (I attribute the differences in empirical and calculated values to be the violation of the $V_P/V_S = 2$ assumption.)

The complex patterns of AVO crossplots from recorded seismic data can be understood using this model-based methodology. In this example, peaks move up and away from the trend (blue), troughs move down and out (gold). This direction of movement is important since it measures a shift in intercept and gradient value which can be defined as a “pore-fluid change vector” or fluid vector.

The fluid vector, reservoir variations, and seismic wavelets

One of AVO's shortcomings alluded to earlier is that single attributes behave more as scalar measurements, whereas crossplotting shows how the two terms interact, defining a fluid vector. Castagna and Smith (1994), Castagna and Swan (1997), and Castagna et al. (1998) displayed the brine-to-gas movement with shale, water-filled, and gas data points from 25 different areas. Castagna and Smith (1994) presented the results in a 1-D display, whereas the other papers displayed the fluid-vector movements through the A - B plane (crossplots). These crossplot papers present generalized fluid-vector movement away from a background trend line for a given sample.

Fluid-vector movement.—Although these analyses are extremely enlightening in terms the mechanics of crossplotting and the classification of AVO responses, they do not emphasize the movements associated with convolved wavelet responses. An example of the complexities associated with a convolved wavelet can be observed in Figure 8 by zooming in on the lower left quadrant, and examining only those points associated with the top of the reservoir (shale over brine sand and shale over gas sand interface.) In order to better see the crossplot movement from shale-wet sand to shale-gas sand, the intercept and gradient sections have been poststack depth converted. One can see how the seismic samples corresponding to the top of the wet sand (the trough) move away from the background trend when gas charged. The crossplot pairs in Figure 8 have been color coded by depth. Sample-by-sample movement from wet to gas sand is not parallel, and larger fluid-vector movements occur for the samples associated with the larger intercept trough excursions, which taper off in magnitude and vary in direction as the samples move away from the largest amplitudes in the trough. Although not shown, the time-based

version of this crossplot looks nearly identical to the depth-based crossplot, which indicates that the effects of delay time are a secondary factor in the fluid-vector movement.

There are many factors that synergically affect the fluid vector. Most of them involve reservoir variations such as changes in porosity, water saturation, thickness, reservoir cleanliness, etc.; others involve seismic wavelet effects. For this tutorial, I do not attempt to itemize and discuss all of the factors, but I focus on two that are routinely encountered—thickness variations and wavelet (bandwidth) variations—and then comment on petrophysical and lithology variations.

Thickness variations.—To emphasize thickness variations, the cleaner sand members of the modeled reservoir have been reduced in thickness by 50 and 75%, and *A* versus *B* crossplots constructed. These crossplots are from time-based data. Although this procedure is intended to demonstrate how changes in thickness will alter the appearance of a crossplot, as a secondary factor it incorporates variations in sand percentage since only the cleaner sand members were reduced. Figure 9 presents the crossplot results using a 600-ms window surrounding the modeled reservoir (Figures 9a, 9c, and 9e) and a zoom of just the shale-sand interface at the top of the reservoir (Figures 9b, 9d, and 9f). With the 600-ms crossplot window, one can see that background trend is invariant, and that variations in reservoir thickness cause different movement from the background trend. While the crossplot in Figure 9a for the original reservoir thickness has a well-defined and somewhat symmetric movement away from the background trend, the half thickness crossplot (Figure 9c) and quarter thickness model (Figure 9e)

have a lopsided appearance. For the crossplots that isolate the shale-reservoir sand response, the differences for the maximum fluid-vector, as well as the direction of movement is striking. As the reservoir is thinned, the maximum fluid vector changes from nearly orthogonal to the background trend to subparallel to the intercept axis. This implies that below tuning (for this model), the intercept variation is dominant, whereas for the thicker reservoir (at or above tuning), the intercept-gradient interaction is more balanced. More importantly, this suite of crossplots indicates that reservoir thickness variations complicate the crossplot response.

Seismic bandwidth considerations.—Another factor affecting the fluid vector is the seismic wavelet (seismic bandwidth). The scale of the reservoir features is quite small in comparison to the seismic wavelet, and some of these intricacies of the reservoir can be partially masked by the larger scale seismic wavelet. Typical seismic wavelets extracted from poststack seismic data are more complex than the simple wavelets used in this modeling exercise. Acquisition variations in the source and receiving parameters, changes in the acquisition environment, as well as data processing procedures all effect the wavelet. For thick blocky sands well above the tuning thickness, these effects may be secondary, but for thinner sands and sands with gradational geologies, the results may be more difficult to analyze using the actual seismic wavelet.

To aid in demonstrating effects of wavelets on seismic crossplotting, the CDP data was bandpass filtered prior to computing the *A* and *B* terms. The *A* and *B* attributes were then cross-plotted. Figures 10a and 10b are, respectively, the unfiltered (4/8–24/48 Hz) and the bandpass filtered (4/8–20/24 Hz) crossplots. Comparison of fluid-vector movements in Figures 10a and Figure 10b illustrate the effects of seismic bandwidth. Other differences can be generated using different wavelets, but for this paper just the simple filter is enough to demonstrate the issue.

Lithologic and petrophysical considerations.—A third factor to consider is the degree of pore fluid or lithologic change. Larger vectors can be expected for larger variations in elastic parameters (V_p , ρ , and σ). For example, in unconsolidated Tertiary rocks, a gas fluid replacement typically shows a larger density, velocity, and Poisson's ratio decrease than an oil fluid replacement does. One would expect to see larger fluid vectors (away from background) for a gas sand than an oil sand. However, if there is gas associated with the oil, the differences may not be that significant. Similarly, increasing the shale or silt content of a reservoir will also affect the movement away from background. Furthermore, there are numerous lithologic and diagenetic effects to consider, most of which lie outside the scope of this tutorial paper.

Therefore, when performing crossplot analysis, *a priori* knowledge from modeling regarding the magnitude of the fluid vector is important. Additionally, since slight variations (small vectors) might be more difficult to observe in crossplots if they do not separate from the background trend, it behooves the analyst to reduce the crossplot scatter of the background trend as much as possible. For this reason, Castagna et al. (1998) recommends a very small window parallel to bedding that contains a constant V_p/V_s . This recommendation confines the spread of

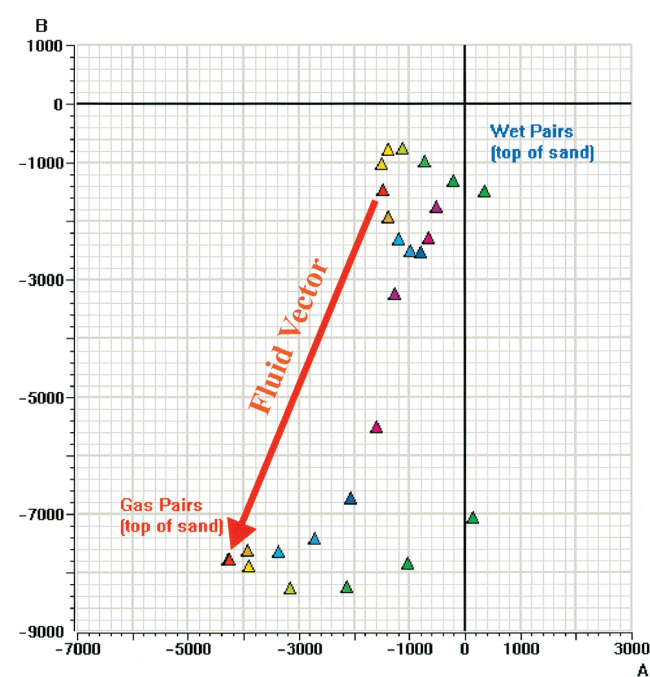


FIG. 8. AVO crossplot of the intercept and gradient using depth-converted data. The data window corresponds to the trough that occurs for the shale-over-sand interface at the top of the reservoir. Intercept-gradient pairs are color coded by depth so one can follow the fluid-vector movement from the wet sand (center) to the gas-charged sand (bottom left corner).

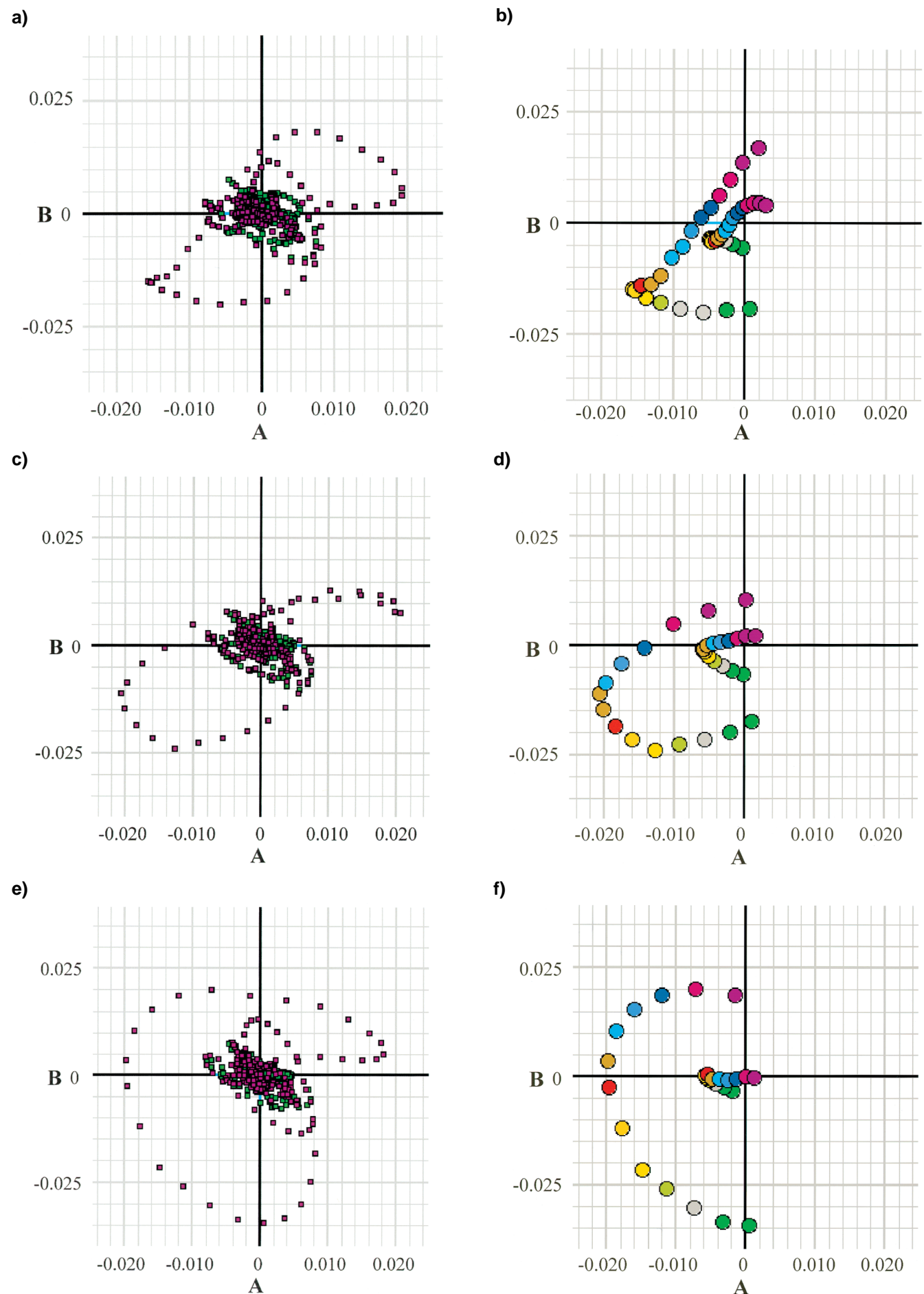


FIG. 9. Time-based crossplot of the intercept and gradient (a), and zoom of the trough fluid-vector movement (b). Time-based crossplot of the intercept and gradient after removing 50% (thinning) of the cleaner sand members in the reservoir (d), and zoom of the trough fluid-vector movement (e). Time-based crossplot of the intercept and gradient after reducing the results in (c) and (d) by another 50% (thinning) of the cleaner sand members in the reservoir (e), and zoom of the trough fluid-vector movement (f).

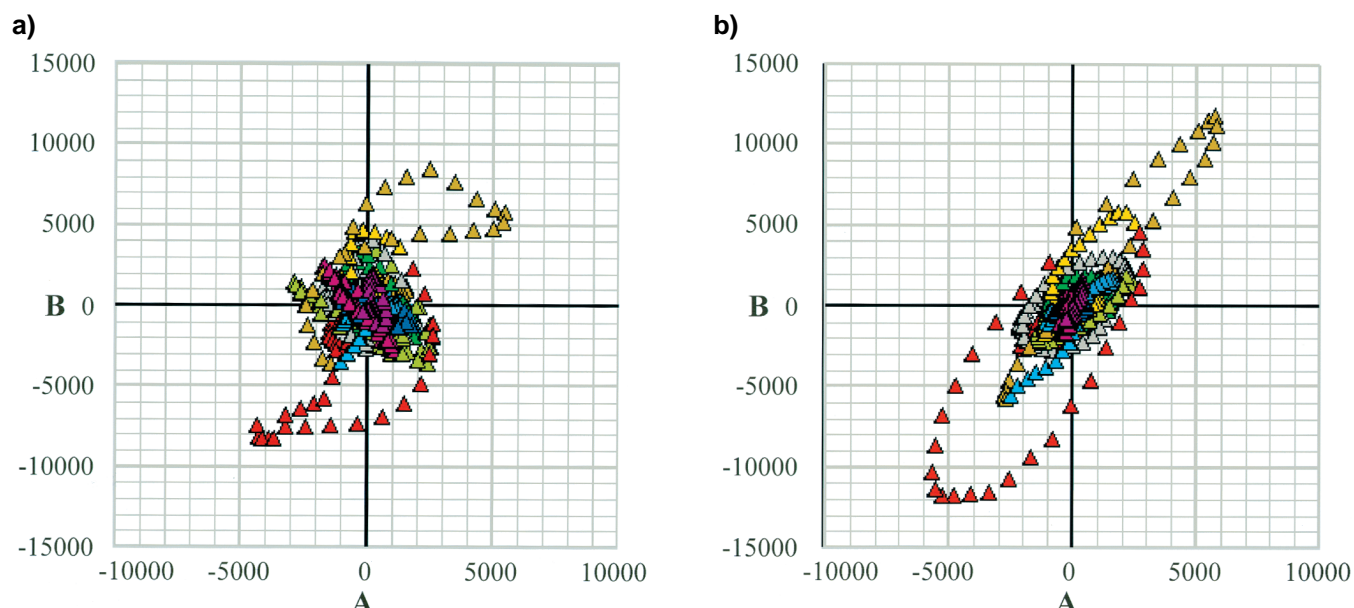


FIG. 10. (a) Time-based crossplot of the intercept and gradient. This is the same as Figures 8 and 9a with different axis scaling. (b) Time-based crossplot of the intercept and gradient, but calculated after applying a 4/8–20/24 Hz filter. The scaling is identical to (a).

the background trend, permitting subtle events the opportunity to stand out.

Comments on fluid vector.—It has been shown that movement from a water-charged to a gas-charged reservoir is not always parallel between nearby geologies, nor is the movement from the background trend always orthogonal to the trend. These points were made using a fairly simple model and wavelet. More complexities should be expected with observed seismic records. To this end, one should always question the validity of attributes that measure the orthogonal distance from the background trend to the anomalous intercept-gradient pairs. Single attributes such as the apparent distance from the fluid line have strong potential for ambiguous results. Better diagnostics of reservoir quality and fluid content will result from using two AVO attributes and crossplotting techniques.

CONCLUSIONS

AVO crossplotting of modeled seismic data derived from well logs with the Biot-Gassmann equations provides a basis for understanding fluid substitution effects on AVO attribute interactions. This understanding should lead to meaningful parameter selection when choosing what attributes to measure, and how to display the crossplot results within a seismic volume. Additionally, the modeling has reconfirmed that AVO crossplotting is a diagnostic tool for identifying hydrocarbons and aiding in AVO data reduction. However, in doing so I have also demonstrated some of the complexities involved with crossplotting.

The ability to crossplot attributes from a 3-D volume permits a geophysicist to high grade subsets of the 3-D survey that warrant detailed inspection of the CDP data. To examine tens of thousands of CDPs is impractical, and crossplotting techniques reduce the amount of CDPs to be inspected by several magnitudes. Crossplotting has become a fundamental process in AVO analysis, just as it is in petrophysical analysis. Comprehending

the intricacies and selection of attributes is essential for successful AVO analysis and improved seismic interpretation.

ACKNOWLEDGMENTS

I thank Paul Beale, John Castagna, Doug Foster, Dan Hampson, Dan Kinman, Brian Russell, and Larry Lines for their review and comments. Additional thanks to Ron Kerr, Tom Fountain, Vince Johnson, and Magda Tobias for their support in data preparation and processing.

REFERENCES

- Aki, K. I., and Richards, P. G., 1980, Quantitative seismology: W. H. Freeman and Co.
- Arbogast, J. S., Franklin, M. H., Butler, M. L., and Thompson, K. A., 1997, Enhancement of “limited” log suites using neural networks, in Coalson, E. B., Osmond, J. C., and Williams, E. T., Eds., Innovative applications of petroleum technology in the Rocky Mountain area: Rocky Mountain Assoc. Geologists, 155–162.
- Castagna, J. P., 1993, Petrophysical imaging using AVO: The Leading Edge, **13**, No. 3, 172–178.
- Castagna, J. P., and Backus, M. M., 1993, Offset-dependent reflectivity—Theory and practice of AVO analysis: Soc. Expl. Geophys.
- Castagna, J. P., and Smith, S. W., 1994, Comparison of AVO indicators: A modeling study: Geophysics, **59**, 1849–1855.
- Castagna, J. P., and Swan, H. W., 1997, Principles of AVO crossplotting: The Leading Edge, **17**, No. 4, 337–342.
- Castagna, J. P., and Swan, H. W., and Foster, D. J., 1998, Framework for AVO gradient and intercept interpretation: Geophysics, **63**, 948–956.
- Domenico, S. N., 1976, Effect of brine-gas mixture velocity in an unconsolidated sand reservoir: Geophysics, **41**, 882–894.
- Foster, D. J., Keys, R. G., and Reilly, J. M., 1997, Another perspective on AVO crossplotting: The Leading Edge, **16**, No. 9, 1233–1237.
- Foster, D. J., Smith, S. W., Dey-Sarkar, S., and Swan, H. W., 1993, A closer look at hydrocarbon indicators: 63rd Ann. Internat. Mtg., Soc. Expl. Geophys., Expanded Abstracts, 731–733.
- Gardner, G. H. F., Gardner, L. W., and Gregory, A. R., 1974, Formation velocity and density—The diagnostic basics for stratigraphic traps: Geophysics, **39**, 770–780.
- Greenberg, M. L., and Castagna, J. P., 1992, Shear-wave velocity estimation in porous rocks: Theoretical formulation, preliminary verifications and applications: Geophys. Prosp., **40**, 195–209.
- Hatchell, P. J., 1993, Comparison of shear-wave sonic logging tools. Presented at SPWLA Shear-Wave Technology Conference.

- Kennett, B. L. N., 1979, Theoretical reflection seismograms for elastic media: *Geophys. Prosp.*, **27**, 301–321.
- Koefoed, O., 1955, On the effect of Poisson's ratios of rock strata on the reflection coefficients of plane waves: *Geophys. Prosp.*, **3**, 381–387.
- Mazzotti, A., 1990, Prestack amplitude analysis methodology and application to seismic bright spots in the Po Valley, Italy: *Geophysics*, **55**, 157–166.
- Murphy, W., Reischer, A., and Hsu, K., 1993, Modulus decomposition of compressional and shear velocities in sand bodies: *Geophysics*, **58**, 227–239.
- Ostrander, W. J., 1984, Plane-wave reflection coefficients for gas sands at nonnormal angles of incidence: *Geophysics*, **49**, 1637–1648.
- Ross, C. P., 1995, Improved mature field development with 3D/AVO technology: *First Break*, **13**, No. 4, 139–145.
- , 1997, AVO and nonhyperbolic moveout: A practical example: *First Break*, **15**, No. 2, 43–48.
- Ross, C. P., and Beale, P. L., 1994, Seismic offset balancing: *Geophysics*, **59**, 93–101.
- Ross, C. P., and Kinman, D. L., 1995, Non-bright spot AVO: Two examples: *Geophysics*, **60**, 1398–1408.
- Shuey, R. T., 1985, A simplification of Zoeppritz equations: *Geophysics*, **50**, 609–614.
- Smith, G. C., and Gidlow, P. M., 1987, Weighted stacking for rock property estimation and detection of gas: *Geophys. Prosp.*, **35**, 993–1014.
- Simmons, J. L., Jr., and Backus, M. M., 1994, AVO modeling and the locally converted shear wave: *Geophysics*, **59**, 1237–1248.
- Verm, R., and Hilterman, F., 1995, Lithology color-coded seismic sections: The calibration of AVO crossplotting to rock properties: *The Leading Edge*, **14**, No. 8, 847–853.

APPENDIX A

A TERSE REVIEW OF AVO

AVO by definition is amplitude variation with offset. It is the measure of seismic amplitude (energy or envelope) across a velocity (NMO) corrected CDP gather from near trace to far trace. It is often performed on a sample-by-sample basis, or in some cases using small windows to account for residual NMO errors or noise. Papers by Koefoed (1955) and Shuey (1985) provide theoretical documentation and definitions, whereas

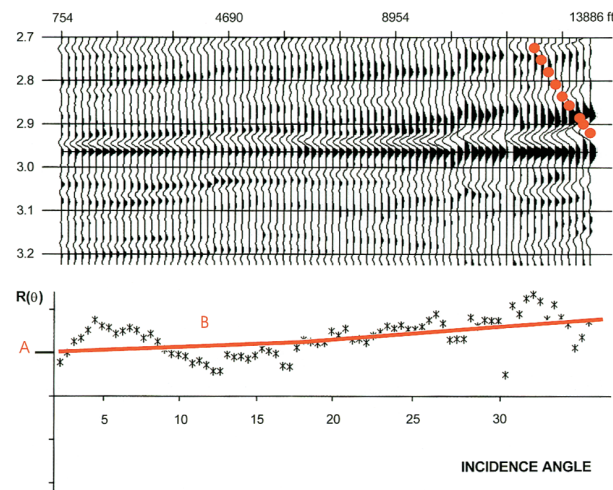


FIG. A-1. NMO-corrected CDP gather from the offshore Gulf of Mexico flexure trend. The event at 2.97 s (peak) demonstrates the AVO response anticipated for 100 ft (30 m) of upper Miocene gas deposits. Near trace is left, far trace right. Amplitude values from the picked trough are plotted as a function of average incident angle (bottom). Gradient and intercept values are determined as shown.

papers by Ostrander (1984), Mazzotti (1990), Ross and Beale (1994), and Ross and Kinman (1995) all present examples of CDPs and subsequent measurements of the CDPs. A good overall review of AVO can be found in Castagna and Backus (1993).

Computational efficiencies in AVO analysis have resulted in two primary AVO attributes: the gradient (B) and the intercept (A). The gradient is determined by assessing the rate of change across the gather, the intercept is the zero-offset amplitude determined by extrapolating the AVO gradient. Figure A-1 illustrates the intercept and gradient measurements on a CDP record. For the NMO-corrected CDP with offsets increasing from left to right, a strong increase in amplitude is observed for the event at 2.97 s. At the near offset 754 ft (230 m), the seismic amplitude of the event is much smaller than the event observed at 13 688 ft (4170 m). By plotting the amplitude of each sample as a function of offset or using available velocity information, average incident angle, A , and B can be determined by regression techniques (see Figure A-1). The reflection coefficient as a function of average incident angle [$R(\theta)$] can be expressed as $R(\theta) = A + B \sin^2(\theta)$. A and B terms are the coefficients discussed in the Aki and Richards equation in Appendix B.

Please note that every seismic event has an AVO response—some have constant amplitude versus offset, some increase with offset, some decrease with offset, and some may reverse phase at mid offset. What makes the AVO technique work is identifying those lithologies or fluid-filled reservoirs that have a unique offset response. For high-porosity clastics, the anomalous AVO response is often associated with hydrocarbon saturation, whereas in lower porosity clastics and in some carbonates, the responses are more often associated with lithology and porosity.

APPENDIX B

DEMONSTRATION THAT THE SPR ATTRIBUTE IS EQUIVALENT TO THE FLUID FACTOR

I claim that the scaled Poisson's ratio change (SPR) attribute in this paper is equivalent to the fluid factor (Smith and Gidlow, 1987). This claim is based on selecting small, structurally conforming windows (equivalent to fat horizon slices) where the V_p/V_s ratio is essentially invariant.

Beginning with the Aki and Richards (1980) representation,

$$R(\langle\theta\rangle) = A + B \sin^2\langle\theta\rangle + C \sin^2\langle\theta\rangle \tan^2\langle\theta\rangle, \quad (\text{B-1})$$

where $R(\langle\theta\rangle)$ is the reflection coefficient as a function of average incident angle θ , with

$$A = \frac{1}{2}(\Delta V_p/\langle V_p \rangle + \Delta \rho/\langle \rho \rangle), \quad (\text{B-2})$$

$$\begin{aligned} B &= \frac{1}{2}\Delta V_p/\langle V_p \rangle - 2(\langle V_s \rangle/\langle V_p \rangle)^2 \\ &\times 2(\langle \Delta V_s \rangle/\langle V_s \rangle + \Delta \rho/\langle \rho \rangle), \end{aligned} \quad (\text{B-3})$$

and

$$C = \frac{1}{2}\Delta V_p/\langle V_p \rangle, \quad (\text{B-4})$$

ΔV_p , ΔV_s , and $\Delta \rho$ are the changes in the compressional velocity, shear velocity, and density, respectively, across the interface. Similarly, $\langle V_p \rangle$, $\langle V_s \rangle$ and $\langle \rho \rangle$ are the averages of the compressional velocity, shear velocity, and density across an interface, respectively.

From Gardner et al. (1974), in most sedimentary basins, small changes in density can be expressed as small changes in (compressional) velocity, such that

$$\Delta \rho/\langle \rho \rangle \approx g V_p/\langle V_p \rangle, \quad (\text{B-5})$$

where g is 1/4. Using equation (B-5), equations (B-2) and (B-3) can be rewritten as equations (B-6) and (B-7), respectively, assuming $\langle V_p \rangle/\langle V_s \rangle$ remains constant:

$$A = \frac{5}{8} \frac{\Delta V_p}{\langle V_p \rangle}, \quad (\text{B-6})$$

or

$$\frac{\Delta V_p}{\langle V_p \rangle} = \frac{8}{5}A, \quad (\text{B-6a})$$

$$B = \frac{4}{5}A - 2\gamma^2 \left(2 \frac{\Delta V_s}{\langle V_s \rangle} + \frac{2}{5}A \right). \quad (\text{B-7})$$

By substituting equation (B-6) into equation (B-7), and letting $\langle V_s \rangle/\langle V_p \rangle = \gamma$,

$$B = \frac{1}{2} \frac{\Delta V_p}{\langle V_p \rangle} - 2 \left[\frac{\langle V_s \rangle}{\langle V_p \rangle} \right]^2 \left(2 \frac{\Delta V_s}{\langle V_s \rangle} + \frac{1}{4} \frac{\Delta V_p}{\langle V_p \rangle} \right), \quad (\text{B-8})$$

which can be further reduced to

$$B = \frac{4}{5}A(1-\gamma)^2 - 4\gamma^2 \frac{\Delta V_s}{V_s}, \quad (\text{B-9})$$

or

$$\gamma \frac{\Delta V_s}{\langle V_s \rangle} = \frac{A}{5}(1-\gamma)^2 - \frac{B}{4\gamma}. \quad (\text{B-9a})$$

From Smith and Gidlow (1987), the fluid factor is defined as

$$\Delta F = \frac{\Delta V_p}{V_p} - 1.16\gamma \frac{\Delta V_s}{V_s}, \quad (\text{B-10})$$

and by substitution of equations (B-6a) and (B-9a), equation (B-10) becomes

$$\Delta F = \left[1.6 - 0.232 \frac{(1-\gamma)^2}{\gamma} \right] A - \frac{0.29}{\gamma} B. \quad (\text{B-11})$$

Generalizing, the fluid factor is then equivalent to

$$\Delta F = \alpha A - \beta B, \quad (\text{B-12})$$

where

$$\alpha = \left[1.6 - 0.232 \frac{(1-\gamma)^2}{\gamma} \right] \quad (\text{B-12a})$$

and

$$\beta = \frac{0.29}{\gamma}. \quad (\text{B-12b})$$

Assuming the traditional γ value of 2, equation (B-12) becomes

$$\Delta F = 1.252A - 0.58B, \quad (\text{B-13})$$

or factoring by k ($k = 2.504$)

$$\Delta F = k(0.50A - 0.23B), \quad (\text{B-14})$$

or

$$k^{-1}\Delta F \approx 0.50A - 0.23B. \quad (\text{B-15})$$

However, from in-situ measurements (whether they are by borehole sonic, borehole seismic, or compressional or shear-wave surface seismic measurements), it is known that γ is not always equal to 0.5, and therefore the coefficients in equation (B-15) are not always 0.5 and 0.23 for α and β , respectively. For example, when $\gamma = 0.42$ (very unconsolidated sediments typical of deepwater tertiary sediments) α and β in equation (B-15) become 0.50 and 0.31, respectively. These are the parameters used for the SPR computation in this paper, which are appropriate for a deepwater V_p/V_s ratio of 2.4 (Poisson's ratio of 0.39).

In closing, it has been demonstrated that for windows where γ is constant, the fluid factor is equivalent to the scaled change in Poisson's ratio attribute.